Journal of Physics D: Applied Physics

PAPER

Nanosecond dielectric barrier discharge on a curved surface in atmospheric air: streamer evolution and aerodynamic perturbations

To cite this article: Longfei Li and Jiangfeng Wang 2022 *J. Phys. D: Appl. Phys.* **55** 055203

IOP Publishing

Journal of Physics D: Applied Physics

J. Phys. D: Appl. Phys. **55** (2022) 055203 (15pp)

https://doi.org/10.1088/1361-6463/ac2fdb

Nanosecond dielectric barrier discharge on a curved surface in atmospheric air: streamer evolution and aerodynamic perturbations

Longfei Li and Jiangfeng Wang*

Key Laboratory of Unsteady Aerodynamics and Flow Control of Ministry of Industry and Information Technology, College of Aerospace Engineering, Nanjing University of Aeronautics and Astronautics, Nanjing 210016, People's Republic of China

E-mail: wangjf@nuaa.edu.cn

Received 29 August 2021, revised 11 October 2021
Accepted for publication 14 October 2021
Published 28 October 2021

Abstract

A curved nanosecond-pulsed dielectric barrier discharge actuator is proposed to fit the flexibly complex surface shape of air vehicles. Streamer evolution and aerodynamic perturbations driven by a single-pulse voltage applied on the anode, where the pulse width is 35 ns and the peak voltage is 14 kV, are numerically studied. Continuity equations that consider 15 species and 34 reactions are solved based on the drift–diffusion approximation. The electron temperature is obtained using the local mean energy approximation method. Discharge characteristics during the voltage-rise, plateau and decay stages are discussed, respectively. The streamer is initiated at 2.2 ns. The maximum electric field is progressively located at the head of the streamer, between the electrodes and in the dielectric layer during the three voltage stages, while the maximum value of electron density is settled at the downstream tip of the driven anode. The electron number density at the streamer head increases at the voltage-rise stage, keeps constant during the voltage-plateau stage, decreases at the beginning of the voltage-decay stage and then increases due to the quenching effect of the excited species. Compared with the discharge on a flat surface, the initial discharge propagation velocity is smaller, while it decreases more slowly during the entire applied voltage. The simulated deposited energy matches the analytical solution well. Aerodynamic perturbations are investigated by solving the compressible Navier–Stokes equations. The ambient air is rapidly heated to the maximum temperature of 1883 K within 0.04 μs. The temperature rise remains greater than 1000 K for 0.32 μs and greater than 500 K for 21.6 μs. A 'semiring-like' compression wave is formed from the discharge region; the propagation speed decreases as it propagates away from the wall and then converges to 345 m s^{-1} at 13 μs. High-speed flows are rapidly induced at the beginning, and two vortexes are formed successively due to the interaction between the flow induced by the actuator and the backflow induced by the compression wave.

Keywords: nanosecond dielectric barrier discharge, plasma excited aerodynamics, numerical simulation

(Some figures may appear in colour only in the online journal)

* Author to whom any correspondence should be addressed.

1. Introduction

Dielectric barrier discharge (DBD) is one of the most potential active flow control technologies using plasma [1–6]. Representative advantages are generally classified as fast response time (<0.1 ms), no moving parts and its adaptability for a wide speed range of air vehicles. Attention is also presently being paid to ignition [7] and plasma-assisted combustion [8] for better performance of engines in the field of aerospace. The widely used asymmetric DBD consists of a grounded electrode embedded in the dielectric layer and a driven electrode contact with ambient air. An alternating current (AC) voltage is applied on the driven electrode, and the induced airflow due to the dominant effect of the body force is observed. Limited to locally insufficient velocity, it is rarely employed to control flows with high Reynolds numbers as well as high velocities. The nanosecond-pulsed DBD (NS-DBD) was proposed in 2009 [9], which is capable of controlling flows even at supersonic/hypersonic speed [10]. A compression wave is rapidly formed due to the effect of ultrafast heated ambient air resulting from the nanosecond discharge, which interacts with the flow field.

Experiments are widely carried out for NS-DBD and the corresponding aerodynamic perturbations [11], but due to the limitations of the performances of devices, numerical studies are still indispensable for one to obtain quantitative temporal and spatial results in more detail. For discharge computations, the particle-in-cell model [12–15] and Monte Carlo model [16] are extremely computationally costly under atmospheric conditions, while the fluid-based model is mostly employed, where the species in the computational domain are summatively reduced as positive ions, negative ions, electrons and neutral species, or even further reduced. Unfer [17] proposed a two-dimensional model to compute a discharge and flow field by coupling the momentum and energy transfer from a fluid-based model, which considered positive ions, electrons and neutral species, to the compressible Navier–Stokes equations. An asymmetrical NS-DBD actuator on a flat surface is simulated and the results are in agreement with experiments [18]. Wang [19] numerically studied the effect of energy and body force, and induced the flow field of NS-DBD on a flat surface in atmospheric air. A fluid-based model that considered positive and negative ions and electrons was employed, and the results showed reasonable agreement with experimental shadow images. Che [20] performed a comparative study on discharge characteristics and aerodynamic perturbations between air under atmospheric and near space conditions at a certain altitude of 20 km using a fluid-based model consisting of positive ions and electrons. Joule heating and body force were considered for an NS-DBD on a flat surface, and a 'point explosion' was observed rather than a 'region explosion' in near space. The fluid-based model is also employed by Zhang [21, 22] to study the effect of pressure, temperature and gas velocity. The plasma morphology and gas heating are analyzed and considerable trends are proposed for NS-DBD on a flat surface. Despite the fact that the computational cost of the fluid-based model is relatively lower, which is potentially realizable for three-dimensional modelling, and it is fully coupled with the Navier–Stokes equations, compared with a physics-based model that considers a kinetics scheme, limitations still appear because it is highly parametric dependent and the evolution of detailed species during the discharge process is neglected. Xu [23] proposed a kinetics scheme of seven species and nine reactions and the effects of configurations of the exposed surface of the driven electrode [24], geometry and waveform of voltages [25] on NS-DBD on a flat surface were investigated. The results show that the reduced electric field of the serrated electrode is the greatest as well as the strength of the compression wave and its propagation speed, while results of the semicircular electrode are the weakest. The geometry of both electrodes has little effect on discharge, while higher discharge characteristics are obtained using a shorter pulse-rising time. A kinetics scheme of 17 species and 54 reactions is proposed [26] and employed by Ahn to investigate the evolution of charged particles, electric field and electron energy of NS-DBD on a flat surface. Different physical properties in corresponding plasma regions are presented [27]. Zhang [28] comparatively studied the discharge characteristics of NS-DBD on a flat surface using four kinetics schemes of 31 species/99 reactions, 28 species/85 reactions, 23 species/50 reactions and 15 species/42 reactions, respectively, and compared them with the results of the fluid-based model. Similar discharge energy is obtained and the process of heating release is qualitatively presented. Zhu [29] proposed a kinetics scheme of 16 species and 44 reactions to simulate the discharge process and aerodynamic perturbations. Another kinetics scheme of 15 species and 34 reactions that considered fast gas heating effects is modeled to study the morphology, aerodynamic perturbations and reactively released energy [30]. Contributions of specific reactions are presented and the ambient air is heated with a rapid temperature rise of up to 1170 K [31]. Simulations are also carried out for ionization wave discharges compared with measurements [32]. Despite expensive computational costs, more physical results are obtained and more details of discharges are presented by the physics-based model.

Other methods are also employed for computing the plasma-excited flow field in published investigations. Phenomenological methods are employed by Zhao [33], Li [34] and Wojewodka [35], where the empirical or semiempirical power distribution is used as the energy source. The computational cost is quite low compared with the previously mentioned methods, but the process of discharge cannot be presented and the accuracy is low. Takashima [36] and Zheng [37, 38] reduce the two-dimensional drift–diffusion equations to a quasi-one-dimensional self-similar equation system for the near-wall electric field components parallel and perpendicular to the surface, which is numerically more convenient for fitting complex configurations, but the accuracy of the results is highly parametric dependent.

Despite the massive investigations that have been performed, studies of NS-DBD on curved surfaces using the accurate physics-based model are not yet reported. In this paper, an NS-DBD actuator embedded in a dielectric layer with a curved surface is proposed and simulated. A physics-based model with 15 species and 34 reactions coupled with Poisson's equation and Helmholtz equations is solved. A single nanosecond-pulsed voltage with a peak voltage of 14 kV and pulse width of 35 ns is applied on the driven electrode. Evolution of the electric field, electron number density and energy deposition are analyzed. The discharge propagation velocity is analyzed and compared with the discharge on the flat surface. The distribution of deposited energy along the streamer is also studied and compared with the flat discharge as well as the analytical solution. Furthermore, the aerodynamic perturbations are studied by solving the compressible Navier–Stokes equations. The responses of temperature, pressure and flow field are separately analyzed.

2. Methodology

2.1. Governing equations

2.1.1. Discharge. Behavior of the charged, neutral and excited species is described by the continuity equations. For the ith species,

$$\frac{\partial n_i}{\partial t} + \nabla \cdot \boldsymbol{\Gamma}_i = S_i + S_{\mathrm{ph},i}, i = 1, 2, \ldots, N_{\mathrm{total}} \tag{1}$$

the flux term $\boldsymbol{\Gamma}_i$ is given based on the drift–diffusion approximation

$$\boldsymbol{\Gamma}_i = \mu_i n_i \boldsymbol{E} - D_i \nabla n_i \tag{2}$$

where n_i is the number density, S and S_{ph} are the source terms of chemical reactions and the photoionization, respectively, μ_i and D_i are the mobility and diffusion coefficient of charged species and $\boldsymbol{E}$ denotes the electric field.

The electron energy is calculated by the energy conservation equation:

$$\frac{\partial n_\varepsilon}{\partial t} + \nabla \cdot \boldsymbol{\Gamma}_\varepsilon = -\boldsymbol{\Gamma}_\varepsilon \cdot \boldsymbol{E} - Q_\varepsilon \tag{3}$$

$$\boldsymbol{\Gamma}_\varepsilon = -\mu_\varepsilon n_\varepsilon \boldsymbol{E} - D_\varepsilon \nabla n_\varepsilon. \tag{4}$$

The photoionization source term in the continuity equation is calculated using a three-term Helmholtz model, which is described in detail in [39, 40]

$$S_{\mathrm{ph}} = \sum_i S_{\mathrm{ph},i} \tag{5}$$

$$\nabla^2 S_{\mathrm{ph},i} - (\lambda_i p_{\mathrm{O}_2})^2 S_{\mathrm{ph},i} = -A_i p_{\mathrm{O}_2}^2 I \tag{6}$$

$$I = \xi \frac{p_{\mathrm{q}}}{p + p_{\mathrm{q}}} \alpha \mu E n_{\mathrm{e}} \tag{7}$$

where α is the Townsend ionization coefficient, μE denotes the drift velocity of electrons, p is the pressure, and p_{q} and p_{O_2} indicate the quenching pressure of the excited species $\mathrm{C}^3\Pi_{\mathrm{u}}$ and the partial pressure of O_2.

The coupled electric field is calculated by the Poisson's equation as follows:

$$\nabla \cdot (-\varepsilon_0 \varepsilon \nabla \Phi) = q_{\mathrm{e}} \sum_i Z_i n_i \tag{8}$$

where ε_0 and ε are the permittivity of free space and the relative permittivity of materials, q_{e} is the charge of electrons and Z denotes the charge of species.

2.1.2. Aerodynamics. Aerodynamic perturbations are described by solving the compressible Navier–Stokes equations, which are given by:

$$\frac{\partial \boldsymbol{W}}{\partial t} + \frac{\partial \boldsymbol{E}}{\partial x} + \frac{\partial \boldsymbol{F}}{\partial y} = \frac{\partial \boldsymbol{E}_v}{\partial x} + \frac{\partial \boldsymbol{F}_v}{\partial y} + \boldsymbol{Q} \tag{9}$$

$$\begin{gathered}
\boldsymbol{W} = \begin{bmatrix} \rho \\ \rho u \\ \rho v \\ \rho E \end{bmatrix} \boldsymbol{E} = \begin{bmatrix} \rho u \\ \rho u^2 + p \\ \rho u v \\ \rho u H \end{bmatrix}, \boldsymbol{F} = \begin{bmatrix} \rho v \\ \rho v u \\ \rho v^2 + p \\ \rho v H \end{bmatrix} \\
\boldsymbol{E}_v = \begin{bmatrix} 0 \\ \tau_{xx} \\ \tau_{xy} \\ u\tau_{xx} + v\tau_{xy} + q_x \end{bmatrix}, \boldsymbol{F}_v = \begin{bmatrix} 0 \\ \tau_{yx} \\ \tau_{yy} \\ u\tau_{yx} + v\tau_{yy} + q_y \end{bmatrix} \\
\boldsymbol{S} = \begin{bmatrix} 0 \\ 0 \\ 0 \\ S_{heat} \end{bmatrix}
\end{gathered} \tag{10}$$

where ρ and p are the density and pressure of air, u and v are the velocity in the x and y directions, respectively, and E and H are the total energy and total enthalpy of unit mass. The shear stress terms are described as follows:

$$\begin{aligned}
\tau_{xx} &= \mu \left[-\frac{2}{3} (\nabla \cdot \boldsymbol{V}) + 2 \frac{\partial u}{\partial x} \right] \\
\tau_{xy} &= \tau_{yx} = \mu \left(\frac{\partial u}{\partial y} + \frac{\partial v}{\partial x} \right) \\
\tau_{yy} &= \mu \left[-\frac{2}{3} (\nabla \cdot \boldsymbol{V}) + 2 \frac{\partial v}{\partial y} \right] \\
\nabla \cdot \boldsymbol{V} &= \frac{\partial u}{\partial x} + \frac{\partial v}{\partial y}.
\end{aligned} \tag{11}$$

The heat fluxes are calculated by Fourier's law:

$$\begin{aligned}
q_x &= \kappa \frac{\partial T}{\partial x} \\
q_y &= \kappa \frac{\partial T}{\partial y}
\end{aligned} \tag{12}$$

where T is the temperature and κ is the thermal conductivity.

The ideal gas equation of state is employed for the atmospheric air:

$$p = \rho R T \tag{13}$$

where R is the ideal gas constant, namely 8.314 J (mol K)$^{-1}$.

2.2. Kinetics scheme

The atmospheric air in this study is assumed to be a mixture of N_2 and O_2, where the mole fractions are 0.79 and 0.21, respectively. A detailed kinetics scheme of 46 species

Table 1. The kinetics scheme for NS-DBD.

No.	Reaction	Rate constant	Reference
1	$e + N_2 \leqslant e + e + N_2{}^+$	$f\,(\sigma, E/N)$	[46]
2	$e + O_2 \leqslant e + e + O_2{}^+$	$f\,(\sigma, E/N)$	[47]
3	$e + N_2 \leqslant e + N_2(A^3\Sigma_u)$	$f\,(\sigma, E/N)$	[46]
4	$e + N_2 \leqslant e + N_2(B^3\Pi_g)$	$f\,(\sigma, E/N)$	[46]
5	$e + N_2 \leqslant e + N_2(C^3\Sigma_u)$	$f\,(\sigma, E/N)$	[46]
6	$e + O_2 \leqslant e + O + O$	$f\,(\sigma, E/N)$	[43, 47]
7	$e + O_2 \leqslant e + O + O(^1D)$	$f\,(\sigma, E/N)$	[43, 47]
8	$N_2{}^+ + N_2 + M \leqslant N_4{}^+ + M$	$5 \cdot 10^{-29}$	[42, 43]
9	$N_4{}^+ + O_2 \leqslant O_2{}^+ + N_2 + N_2$	$2.5 \cdot 10^{-10}$	[42, 43]
10	$N_2{}^+ + O_2 \leqslant O_2{}^+ + N_2$	$6 \cdot 10^{-11}$	[42, 43]
11	$O_2{}^+ + N_2 + N_2 \leqslant O_2{}^+N_2 + N_2$	$9 \cdot 10^{-31}$	[42]
12	$O_2{}^+N_2 + N_2 \leqslant O_2{}^+ + N_2 + N_2$	$4.3 \cdot 10^{-10}$	[42]
13	$O_2{}^+N_2 + O_2 \leqslant O_4{}^+ + N_2$	10^{-9}	[42]
14	$O_2{}^+ + O_2 + M \leqslant O_4{}^+ + M$	$2.4 \cdot 10^{-30}$	[42, 43]
15	$e + O_2 + O_2 \leqslant O_2{}^- + O_2$	$2 \cdot 10^{-29}(300/T_e)$	[42]
16	$e + O_2 \leqslant O^- + O$	$f\,(\sigma, E/N)$	[47]
17	$O^- + O \leqslant e + O_2$	$1.4 \cdot 10^{-10}$	[48]
18	$O_2{}^- + O \leqslant e + O_2 + O$	$1.5 \cdot 10^{-10}$	[48]
19	$e + N_4{}^+ \leqslant N_2 + N_2\,(C^3\Sigma_u)$	$2.3 \cdot 10^{-6}(300/T_e)^{\,0.53}$	[48]
20	$e + N_2{}^+ \leqslant N + N$	$1.8 \cdot 10^{-7}(300/T_e)^{\,0.39}$	[48]
21	$e + O_4{}^+ \leqslant O + O + O_2$	$1.4 \cdot 10^{-6}(300/T_e)^{\,0.50}$	[42, 43]
22	$e + O_2{}^+ \leqslant O + O$	$2 \cdot 10^{-7}(300/T_e)$	[42, 43]
23	$O_2{}^- + O_4{}^+ \leqslant O_2 + O_2 + O_2$	10^{-7}	[42]
24	$O_2{}^- + O_4{}^+ + M \leqslant O_2 + O_2 + O_2 + M$	$2 \cdot 10^{-25}$	[42]
25	$O_2{}^- + O_2{}^+ + M \leqslant O_2 + O_2 + M$	$2 \cdot 10^{-25}$	[42]
26	$O^- + N_2{}^+ \leqslant O + N + N$	$2 \cdot 10^{-7}(300/T_{gas})^{\,0.50}$	[41]
27	$N_2(C^3\Sigma_u) + N_2 \leqslant N_2(B^3\Pi_g) + N_2$	$1 \cdot 10^{-11}$	[43]
28	$N_2(C^3\Sigma_u) + O_2 \leqslant N_2 + O + O[1D]$	$3 \cdot 10^{-10}$	[43]
29	$N_2(C^3\Sigma_u) \leqslant N_2 + h\nu$	$2.45 \cdot 10^{7}$	[42]
30	$N_2(B^3\Pi_g) + O_2 \leqslant N_2 + O + O$	$3 \cdot 10^{-10}$	[43]
31	$N_2(B^3\Pi_g) + N_2 \leqslant N_2(A^3\Sigma_u) + N_2$	$1 \cdot 10^{-11}$	[43]
32	$N_2(A^3\Sigma_u) + O_2 \leqslant N_2 + O + O$	$2.5 \cdot 10^{-12}(T_{gas}/300)^{\,0.50}$	[43]
33	$O[^1D] + O_2 \leqslant O + O_2$	$3.3 \cdot 10^{-11}\exp(67/T_{gas})$	[43]
34	$O[^1D] + N_2 \leqslant O + N_2$	$1.8 \cdot 10^{-11}\exp(107/T_{gas})$	[43]

and 395 reactions is proposed by Kossyi [41], which is only presently available for zero-dimensional computations due to the unacceptable computational cost. Other published kinetics schemes are almost reduced from Kossyi's scheme. In this study, a reduced kinetics scheme of 15 species and 34 reactions proposed by Zhu [30, 31] that models the streamer propagation [42], fast gas heating [43] as well as additional reactions [44] is employed to solve the NS-DBD, which is validated in previous studies [30–32]. The kinetics scheme is illustrated in detail in table 1. Rate constants are calculated based on a two-term approximation Boltzmann equation solver BOLSIG+ [45] with cross sections indicated in the table (units in s^{-1}, $cm^3\,s^{-1}$, $cm^6\,s^{-1}$). Electron temperature T_e is obtained by solving the energy conservation equation. The T_{gas} is the temperature of gas (units in K).

2.3. Mean electron energy

The local field approximation (LFA) and the local mean energy approximation (LMEA) are two methods used to describe the mean electron energy. The computational cost using LFA is smaller due to the fact that the transportation coefficients are only related to the reduced electric field and there is no need to solve the energy conservation equation: namely, the electron energy is assumed to be instantly in equilibrium with the varying electric field. Previous studies show that a loss of accuracy occurs on the NS-DBD at the fast-ionization streamer head and the bottom of the streamer close to the dielectric surface [31]. For better accuracy of results, the LMEA is employed in this study, which is more physical and solves the energy conservation equation to obtain the electron energy, even if at greater computational cost.

2.4. Coupling strategy

Because of the big difference in the time scale between the discharge process (nanosecond time scale) and the aerodynamic responses (microsecond time scale), the effect of perturbated quiescent air on the discharge process is negligently small. Therefore, a one-way (loose) coupling strategy is performed, where the discharge process is firstly solved while the perturbated flow field is calculated based on the results of discharge to avoid the ‘stiff problem’ and unexpected computational consumptions; this strategy is also employed by previous studies [20].

2.5. Validation

Calculations of the discharge process and flow field are validated separately in previous publications. The results show great agreement with benchmark cases of discharges and excellent performance on shock wave capture.

The PASSKEy code proposed by Zhu *et al* is employed to solve the discharge process; this was previously validated with a benchmark case of streamer propagation for a point-to-plate configuration [30]. Poisson’s equation and Helmholtz equations are semi-implicitly solved by a preconditioned conjugate-gradient solver [49, 50]. An explicit UNO3 scheme [51] (third order in time and space) coupled with the Strang operator for spatial splitting and a second-order central discretization [52] are employed for the drift and diffusion term correspondingly. The time evolution of electron density along the axis of symmetry and the streamer morphology is greatly consistent with [53]. Since there is strictly no benchmark case of an atmospheric pressure surface streamer, a computation is performed using Soloviev’s [54] studies. The electric field at a specific time moment and the current evolution match well.

A home-made Navier–Stokes solver is used in this study to compute the perturbated flow field, which is described in detail and previously validated [55–58]. The Reynolds-averaged Navier–Stokes equations closed by the k–ω SST turbulence model [59] are solved. The second-order AUSM+ scheme [60] is employed for spatial discretization and the five-step Runge–Kutta method is used for temporal discretization. Non-reactive hypersonic flows with different mach numbers around a cylinder are solved; the shock wave and heat flux on the wall are greatly coincident with experiments [61]. The shock-induced combustion flow is also solved. The shock wave is also accurately captured compared with experimental data [62]. The detailed validations are not included in this paper.

3. Numerical setup

3.1. Geometries and meshes

The proposed NS-DBD actuator is embedded in the dielectric layer on the semicircular surface with a radius of 6.35 mm. A zoom-in view is shown in figure 1. The blue area is the dielectric layer with a thickness of 0.3 mm and a relative permittivity of 3.8. The red area indicates the anode with a width of 4.35 mm in the horizontal direction, which is driven by a single pulsed nanosecond voltage. The purple area is the cathode, which is a grounded electrode. The thickness of electrodes is 37.5 μm. The green area is the ambient part of the plasma area, which is not completely shown in the schematic.

The computation domain for discharge is entirely 40 mm $\times$ 80 mm, as shown in figure 2. Structured square cells are employed for the streamer region, which are uniformly sized to 6 μm $\times$ 6 μm. Other cells are generated by extrapolation with a growth rate of 1.1 in both the x and y directions. The cell number is about 2.7 million.

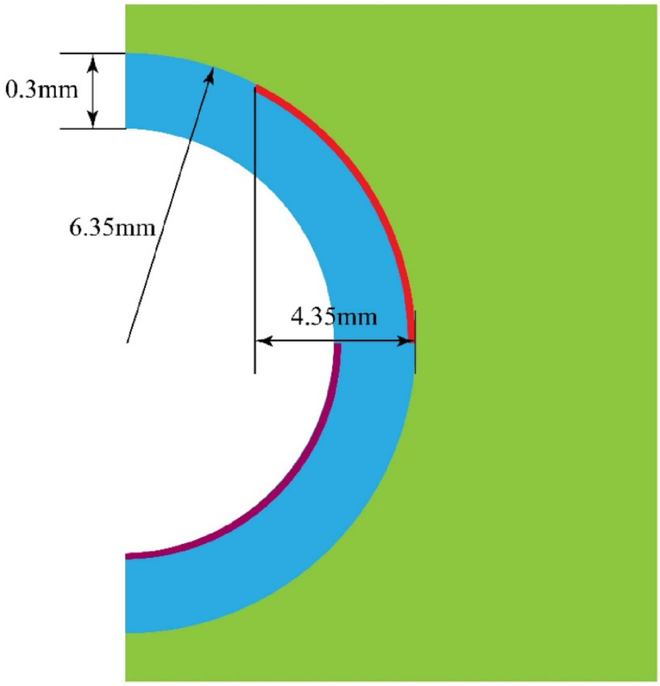

Figure 1. A schematic of the NS-DBD actuator on the curved surface.

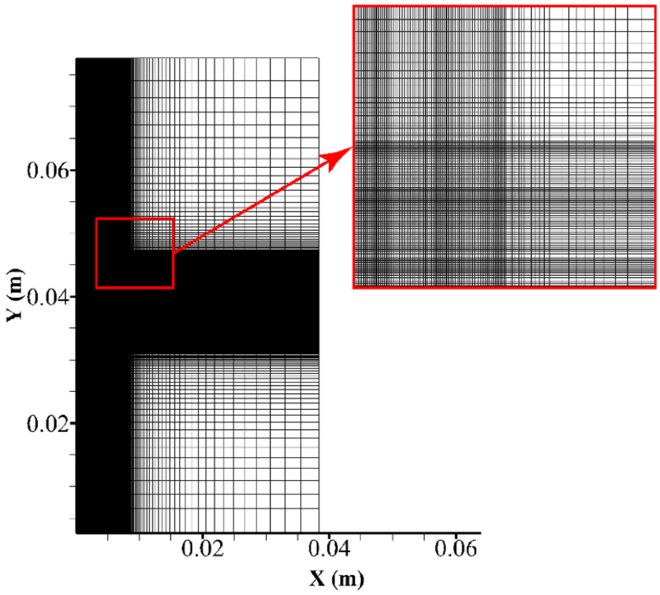

Figure 2. Mesh for discharge calculation.

A different mesh is employed for the perturbated flow field computation due to different requirements of cell size and to reasonably save the computation consumption, which is shown in figure 3. The cell size of the ambient region of the streamer is uniformly set to 20 μm $\times$ 20 μm. The total cell number is 31 680. The energy source of the discharge is transmitted to the mesh of the flow field by a linear interpolation in space.

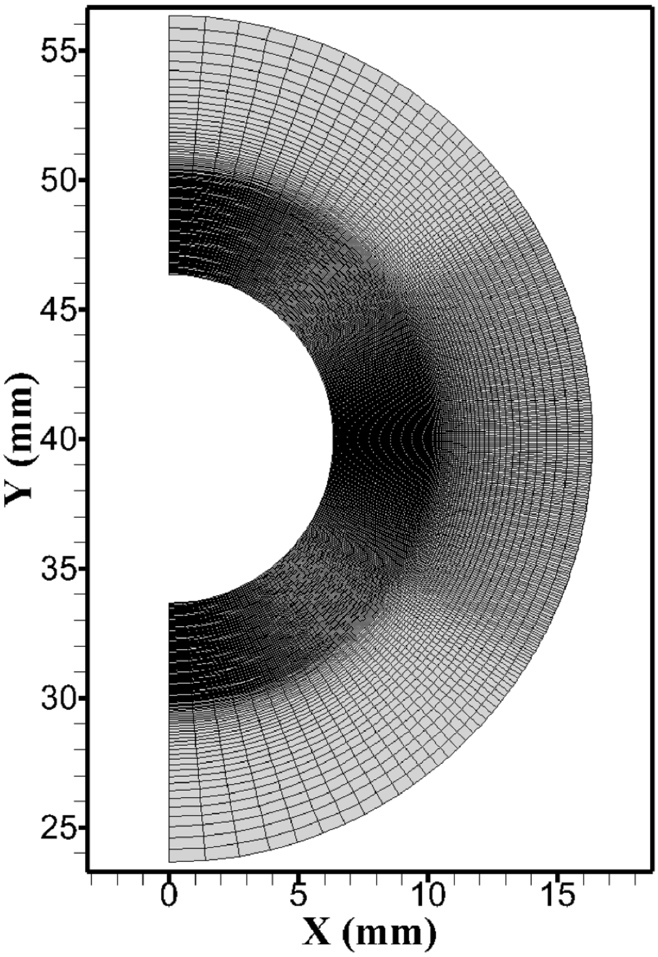

Figure 3. Mesh for aerodynamic calculation.

Table 2. Boundary conditions for continuity equations of species.

Boundary condition	Internal normal direction	External normal direction
Electron	$\partial \boldsymbol{\Gamma}_e / \partial n = 0$	$\boldsymbol{\Gamma}_e = -\gamma \boldsymbol{\Gamma}_i$
Ion	$\partial \boldsymbol{\Gamma}_i / \partial n = 0$	$\boldsymbol{\Gamma}_i = 0$

3.2. Boundary conditions and initial conditions

For Poisson's equation in discharge computation, the Dirichlet boundary condition is applied on metal surfaces, where $\Phi = U(t)$, while the Neumann boundary condition is applied on nonmetal surfaces, where $\partial\Phi/\partial n = 0$. For the Helmholtz equations for photoionization computation, the source term is equal to 0 on boundaries. The boundary conditions for continuity equations of species in the external normal direction and internal normal direction are performed differently, and are illustrated in table 2. The secondary electron emission is ignored due to its negligible effect on NS-DBD.

For flow field computations, the non-slip adiabatic condition is employed on the wall and the extrapolation condition is applied on other boundaries.

The initial electron number density is $1 \times 10^{10}\ \mathrm{m}^{-3}$; the number densities of other ions are the same meanwhile, to ensure the initial charge is zero. The initial mole fractions of N_2 and O_2 are 0.79 and 0.21 correspondingly. The initial pressure and temperature of the quiescent flow field are 1 atm and 300 K, respectively.

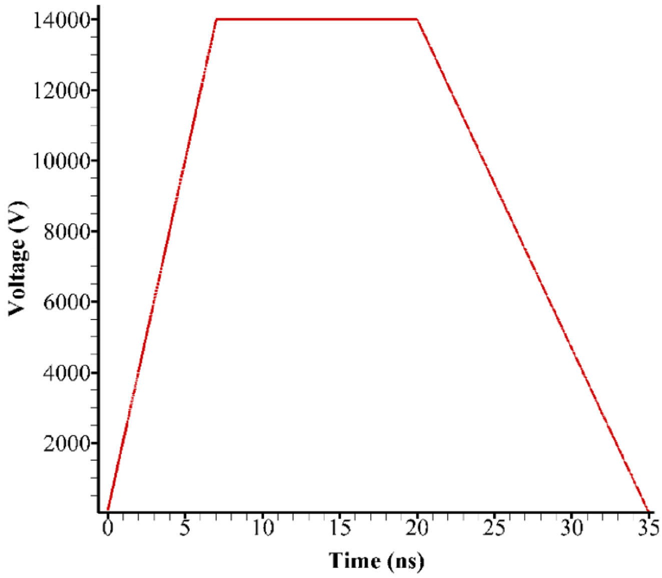

Figure 4. The waveform of the voltage applied on the anode.

3.3. Numerical conditions

A single nanosecond-pulsed voltage with a peak voltage of 14 kV and a pulse width of 35 ns, where the voltage rising time, plateau and decay time are 7 ns, 15 ns and 13 ns, respectively, is applied on the anode, as shown in figure 4, which refers to Unfer's study for an NS-DBD on a flat surface [17].

Atmospheric conditions are applied to the discharge computation, where the pressure is 1 atm and the temperature is 300 K. The transient time step size of the plasma computation determined by the physical process is very small due to specific ultrafast chemical reactions of the kinetics scheme, where the minimum time step is even smaller than 1×10^{-13} s, which is very time consuming. A constant time step size of 5×10^{-9} s is applied for the flow field computation in this study. The discharge and flow field are solved in parallel using the openMP and MPI approach correspondingly on Tianhe One of the National SuperComputer Center in Tianjin (Intel Xeon E5-2690v4 × 2, 128GB, 28 cores per node).

4. Results and discussion

4.1. Discharge process

4.1.1. Evolution of electric field and electron density. The electric fields and electron number density distribution at the voltage-rise stage at specific time moments, namely 1 ns, 2.2 ns, 3 ns and 7 ns, are shown in figures 5 and 6, respectively. Because the sizes of discharge regions at these time moments are different, scales specified for the axis are not the same. At 1 ns before the streamer is initiated, the electric field is the

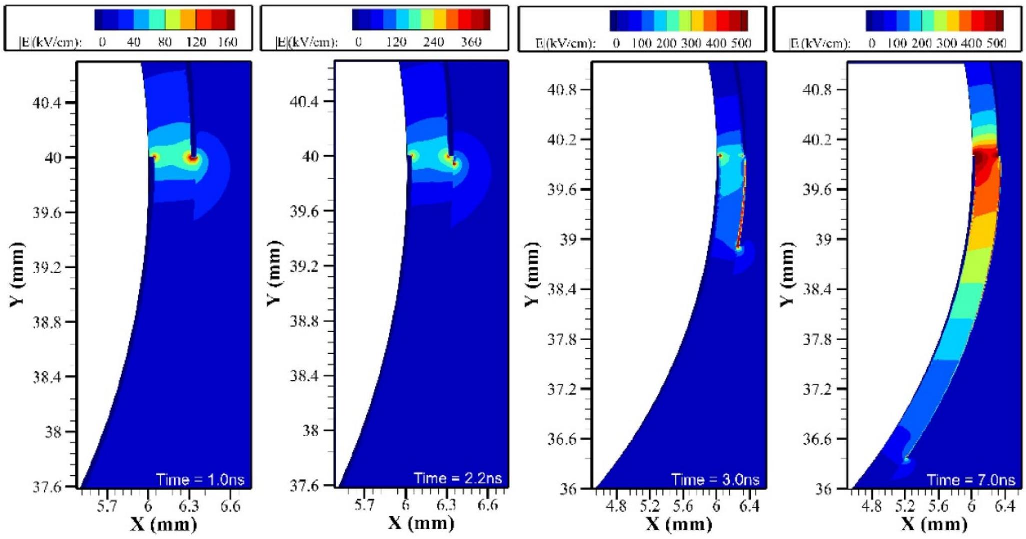

Figure 5. Distribution of electric field at the voltage-rise stage.

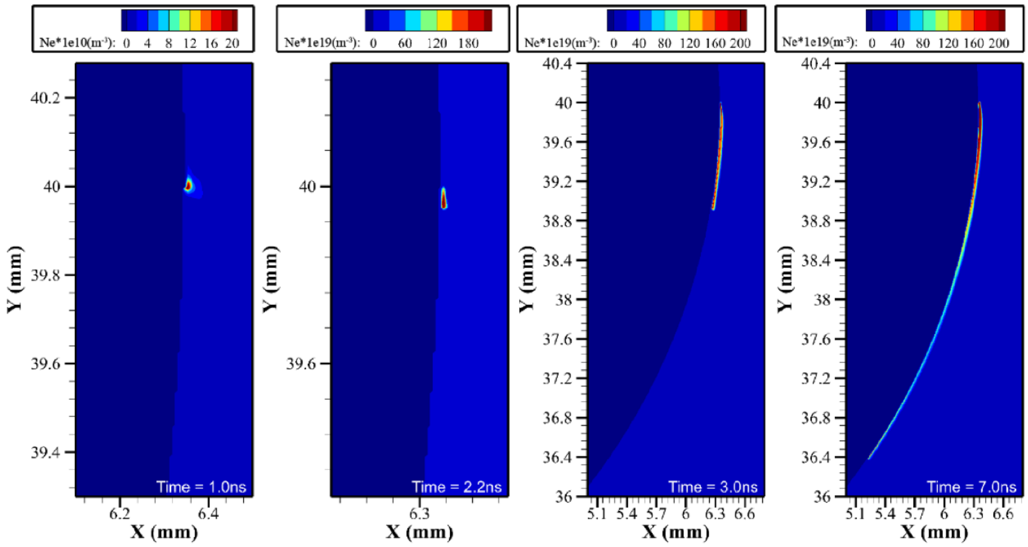

Figure 6. Distribution of electron number density at the voltage-rise stage.

highest at the tip of the anode at the beginning of the discharge, while it decreases progressively as it approaches the cathode. Electrons start to be generated at this moment due to the increasing electric field; the maximum electron number density is about 2.5×10^{11} m^{-3}. The propagation of the streamer starts at approximately 2.2 ns. The electric field increases and the morphology of the streamer deforms due to the change in space charge as a result of ionization reactions. The streamer is generated at the tip of the anode and then propagates along the dielectric surface. The maximum electric field of 585 kV cm^{-1} and the maximum electron density of 3.3×10^{21} m^{-3} both occur at the streamer head. At 3 ns, the streamer head proceeds away from the anode. The maximum electric field seated at the streamer head rises to 794 kV cm^{-1} due to the dominant effect of strong charge-separation processes in the ionization head. The streamer sticks to the curved dielectric surface above the cathode and the thickness of the streamer is approximately uniform. The maximum electron number density is located at the anode due to the locally greater effect of the rise in voltage, which is different from the behavior of the electric field. Until 7 ns, when the voltage reaches the peak, the electric field and electron number density in the streamer channel decrease as the streamer proceeds. The maximum electric field located at the streamer head is 621 kV cm^{-1}, while the maximum electron number density at the tip of the anode is 8.1×10^{21} m^{-3}.

The electric field distribution and electron number density at 14.5 ns and 22 ns, which are the middle and end of the voltage plateau, are presented in figures 7 and 8, respectively. The propagation of the surface-attached streamer slows down from 7 ns. The maximum electric field is no longer located at the streamer head but at the anode. For the streamer head, the electric field decreases to 556 kV cm^{-1} and 540 kV cm^{-1} at these two moments. The location of the maximum electron number density sticks to the anode. The electron number

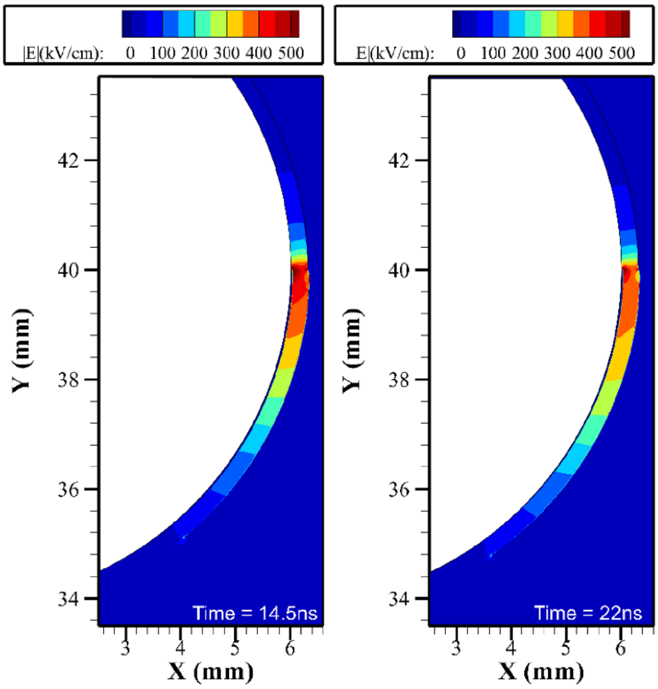

Figure 7. Distribution of electric field at the voltage-plateau stage.

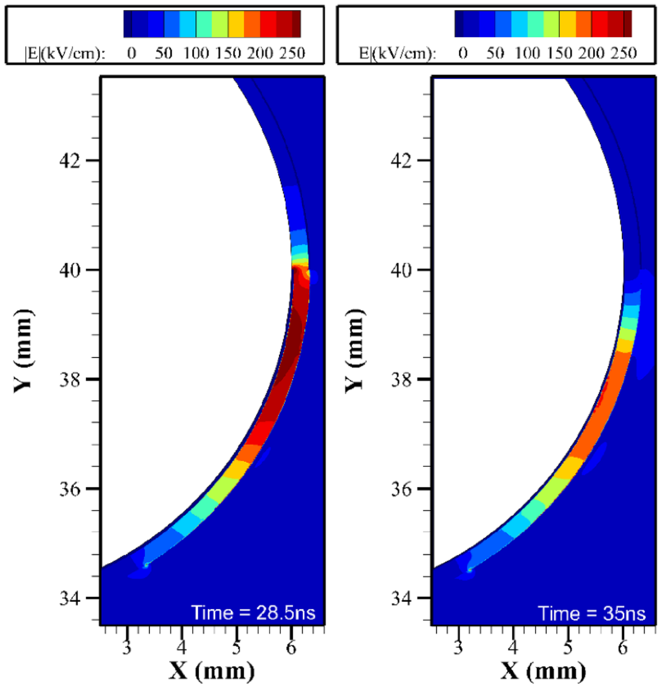

Figure 9. Distribution of electric field at the voltage-decay stage.

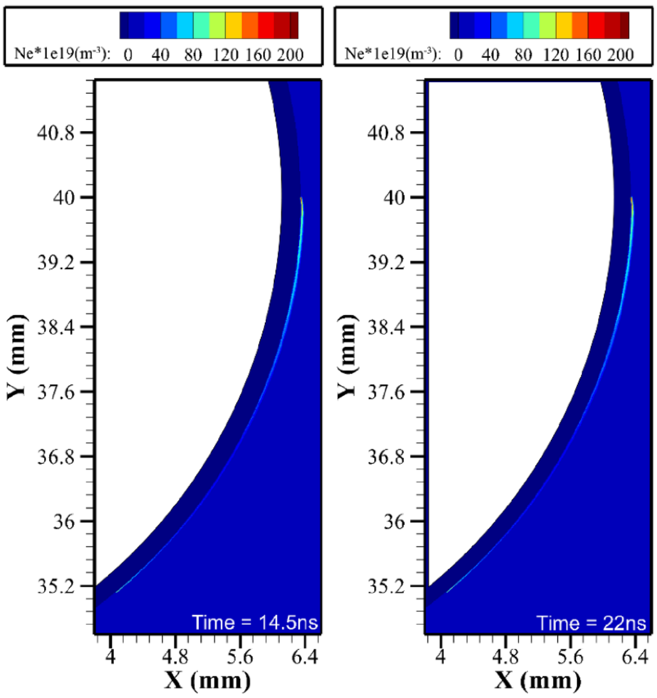

Figure 8. Distribution of electron number density at the voltage-plateau stage.

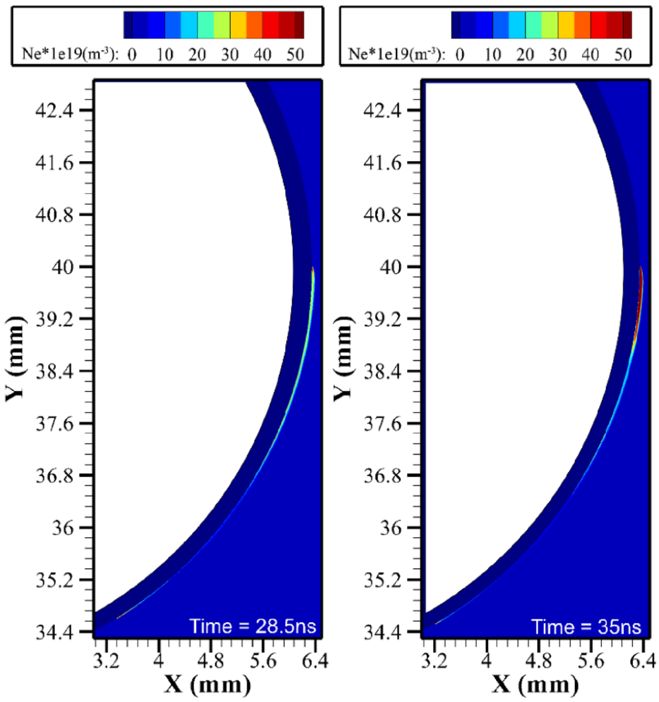

Figure 10. Distribution of electron number density at the voltage-decay stage.

densities remain approximately constant at both the anode and streamer head during the voltage-plateau stage, and are 2.36×10^{21} m^{-3} and 1.50×10^{21} m^{-3} correspondingly.

The 28.5 ns and 35 ns are the middle and end of the voltage-decay stage, and distribution of the electric field and electron number density are shown in figures 9 and 10. The location of the maximum electric field gradually moves to the middle of the dielectric layer. The electric field at the streamer head and the ambience of electrodes decrease simultaneously. At 35 ns, where the applied voltage is 0 V, the electric field of the streamer head reduces to 445 kV cm^{-1}. The electron number density decreases as the electric field decreases until the state of excited species with higher energy levels cannot be maintained due to an insufficient electric field, which results in

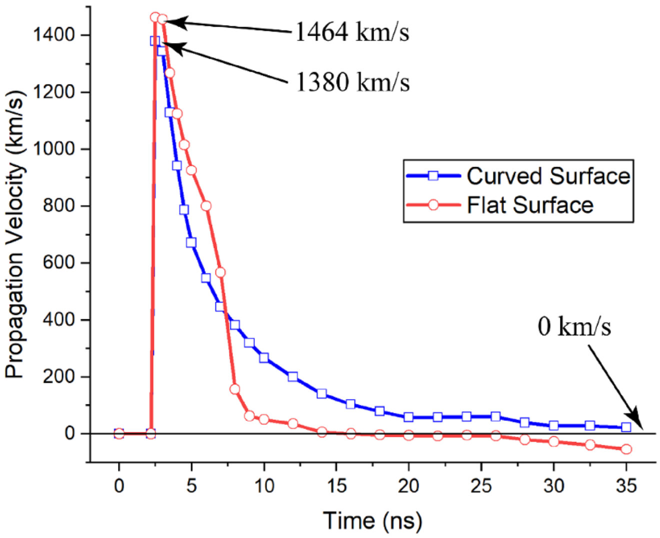

Figure 11. A comparison of the propagation velocity between the curved and flat streamers.

quenching of the excited species to lower levels and the release of energy. Therefore, the electron temperature and electron number density increase unexpectedly.

4.1.2. Streamer dynamics. A simulation for an NS-DBD on a flat surface is also carried out under the same conditions for comparison. The length, thickness and relative locations of the electrodes and dielectric layer are the same as with the curved actuator.

With the same applied voltage, the propagation velocity of the streamer for both the NS-DBD on the flat surface and the curved surface is shown in figure 11. The streamer is simultaneously initiated at 2.2 ns with maximum propagation velocity for both cases. The maximum propagation velocity of the NS-DBD on a flat surface is greater than that on a curved surface. The propagation velocity rapidly decreased as the streamer developed, and the decreasing rate of the flat streamer is greater than the curved streamer. At approximately 16 ns, the propagation velocity of the flat streamer decreases to negative, while the propagation velocity of the curved streamer is always positive, which results in a greater discharge length.

4.2. Discharge energy

For plasma-excited aerodynamic perturbations, the thermal energy of air is transferred from the discharge energy, which is considered differently in published studies. Wang [19] and Che [20] assume that the energy of ions and a fraction of the energy of electrons obtained from the electric field transfer to the gas. Unfer [17] and Abdollahzadeh [63] consider the released energy of electronic excitation, vibrational excitation and the elastic and rotational collisions as the energy of electrons, while the energy of ions is fully included.

In this study, the time evolution of discharge energy in the whole computational domain volume V is analyzed, which refers to Tholin's [64] discussion for glow-to-spark transition. The total power P consists of the power density of Joule heating P_{j} and fast gas heating P_{FGH} and the energy deposition Q and are given as:

$$P = \int_0^V P_{\mathrm{j}} \mathrm{d}V + \int_0^V P_{\mathrm{FGH}} \mathrm{d}V \tag{14}$$

$$Q = \int_0^t P \mathrm{d}t. \tag{15}$$

The evolution of energy deposition and power is shown in figure 12. The discharge is not initiated before 2.2 ns, which is consistent with the analysis of discharge morphology. Then, the discharge power increases and energy deposits with an increasing rate. At 7 ns, the beginning of the plateau, the power reaches the peak and then decreases, where the increment of energy deposition slows down. Until about 27 ns at the voltage-decay stage, the power unexpectedly increases, even though the voltage decays due to the dominant effect of released energy from quenching of the excited species.

The deposited energy at the end of the discharge is compared between the curved discharge and the flat discharge as well as with the analytical method proposed by Soloviev [65–68], as shown in figure 13. The analytical expression assumes the deposited energy decreases linearly along the streamer. The analytical body force is also well established but neglected in this study. The length denotes the horizontal and arc distance to the tip of the anode for the flat and curved discharge correspondingly. The energy is formulated as a function of permittivity, voltage, discharge length, dielectric thickness and breakdown voltage, and matches well with the numerical and experimental results for the flat NS-DBD. The results demonstrate a good agreement between the analytical solutions and numerical results. Similar energy distributions are obtained for both discharges due to the same applied voltage. The discharge length of the curved actuator is greater than the flat discharge, which consists of the trend of the streamer propagation velocity. In the middle of the streamer, the energy decays linearly, except for the ambient of the root and head of the streamer.

4.3. Aerodynamic perturbations

The ultrafast heating-effect gas heating is the main mechanism for plasma-excited aerodynamic perturbations by nanosecond-pulsed voltages. In this study, the aerodynamic flow field is solved through one-way coupling of the spatial distributed power density to the energy source term of the compressible Navier–Stokes equations.

4.3.1. Temperature responses. Evolution of the maximum temperature in the flow field is shown in figure 14 with a zoom-in view given for the first 1 μs. The ambient air is rapidly heated to the highest temperature of 1883 K within 0.04 μs with a temperature rise rate of 4.0 $\times$ 10^{10} K s^{-1}. Then, the temperature decreases with decreasing reduction

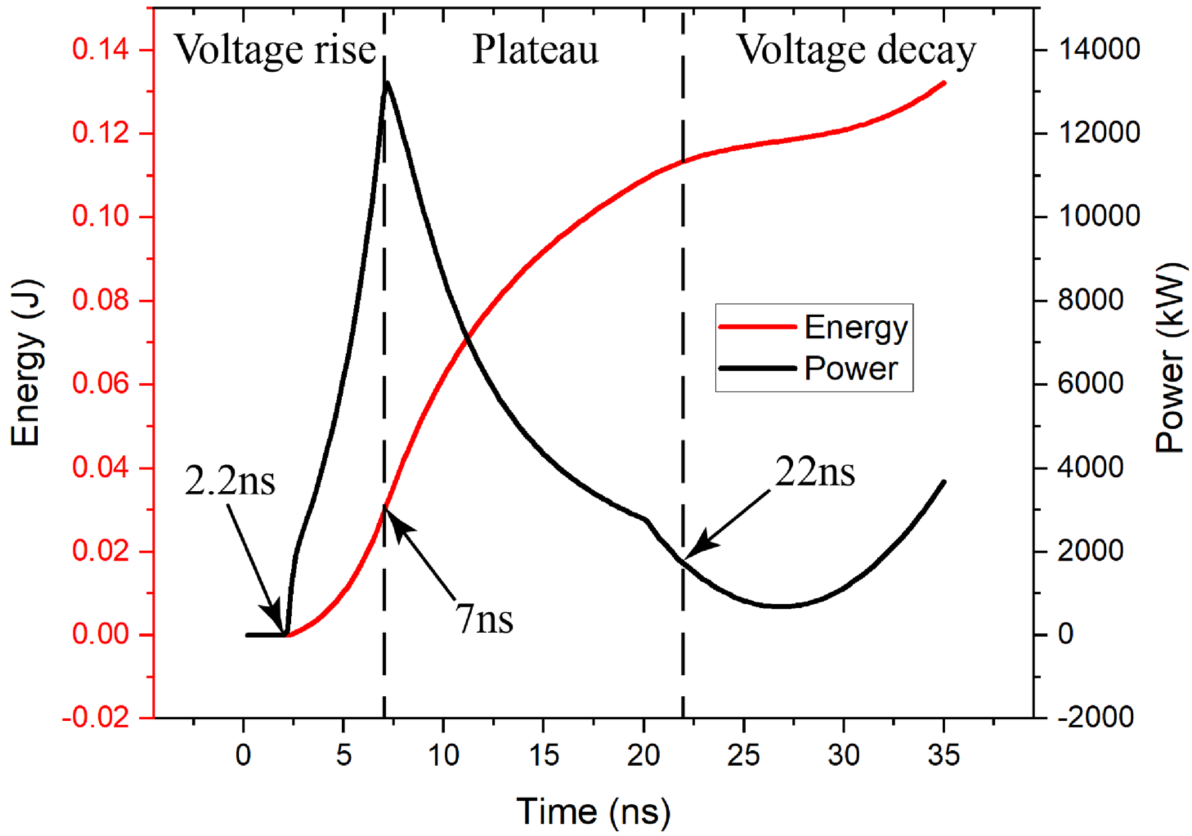

Figure 12. Evolution of energy deposition and power.

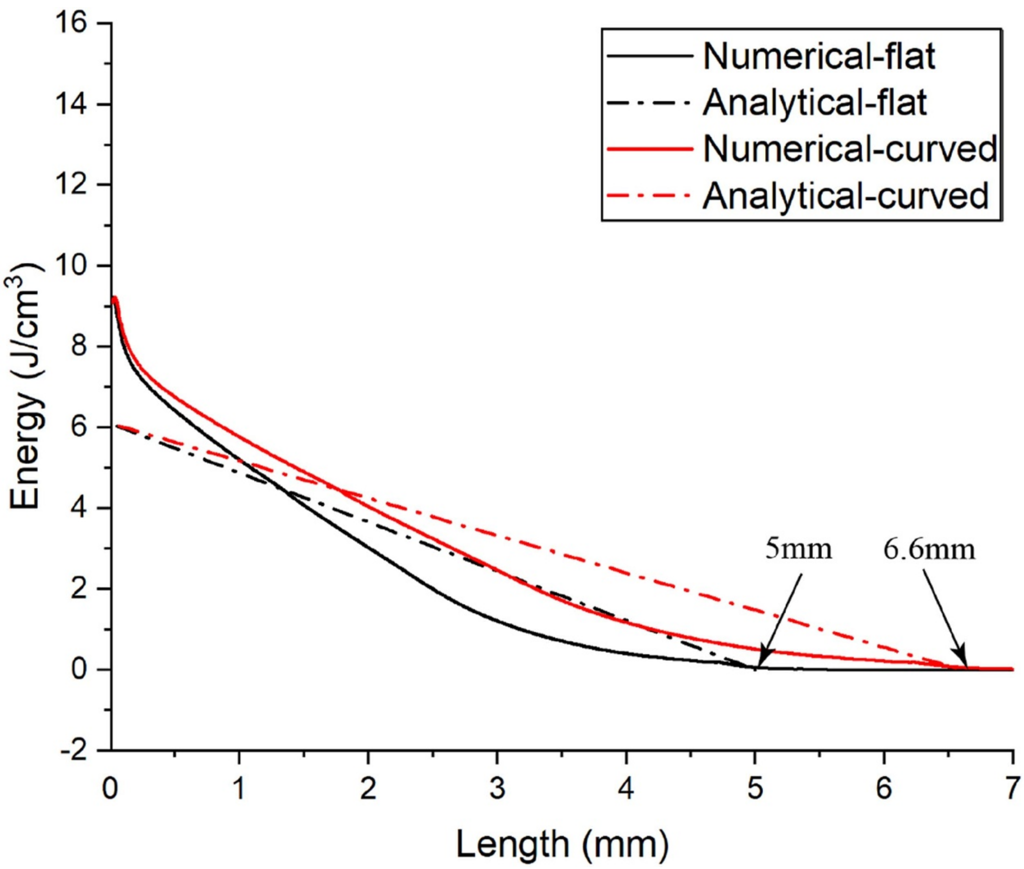

Figure 13. A comparison of deposited energy between the curved and flat discharge.

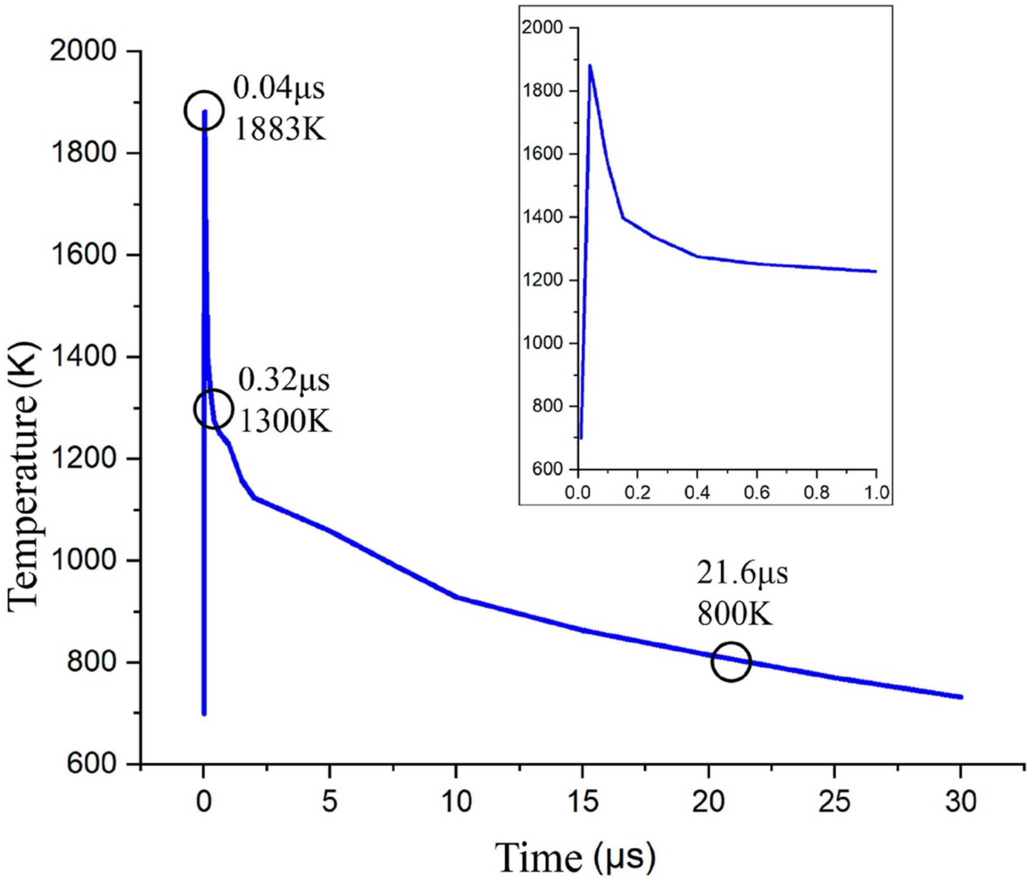

Figure 14. Evolution of the maximum temperature.

rates. The temperature rise of greater than 1000 K is maintained for 0.32 μs and that greater than 500 K is maintained for 21.6 μs.

The temperature distributions of the flow field at 2 μs, 8 μs and 16 μs are shown in figure 15. The region of the highest temperature sticks to the discharge area. The temperature on the compression wave decreases progressively as it propagates further from the wall, where the maximum temperatures on the compression wave are 326.6 K, 312.5 K and 305.2 K, respectively.

4.3.2. Pressure responses. Figure 16 shows the evolution of the propagation speed of the compression wave. The compression wave is initiated before 1 μs with a speed up to about 450 m s^{-1}. Since the compression wave is sufficiently close to the discharge region at the beginning, the strength of the compression wave is very strong. Then, the propagation speed progressively decreases as the shock wave moves away from the wall. Until 13 μs, the propagation speed keeps approximately constant at 345 m s^{-1}, which is very close to the speed of sound.

Pressure distribution at 2 μs, 8 μs and 16 μs is shown in figure 17 sequentially. Non-uniform strength of the compression wave, where the strength is stronger at the front and relatively weaker behind, is presented by regarding the tip of the anode as the center. Because the length of the cathode is relatively longer than the perturbation region at the early stage of the compression wave, the non-uniform energy distribution results in a ‘semiring-like’ compression wave coupled with a curved ‘tail’, which is approximately parallel to the dielectric surface, namely the wall in the flow field. The maximum pressure on these compression waves is 136.2 kPa, 117.0 kPa and 108.1 kPa successively at these time moments.

4.3.3. Velocity responses. High-speed flows are induced by the NS-DBD actuator due to the transiently generated pressure difference. Velocity distribution with streamlines at 0.5 μs, 3 μs, 12 μs and 16 μs successively is presented in figure 18. The velocity on the compression wave is always greater than that inside the wave. At 0.5 μs before the compression wave initiates, the induced velocity is up to 123 m s^{-1}, which is very close to the discharge region. The streamlines are distributed radially. Then, the velocity decreases as the power decays. At 3 μs, the compression wave propagates to a certain distance from the discharge region; backflows are induced due to the pressure difference, where the pressure on the compression wave is higher than that inside the wave. Hereby, streamlines outside the compression wave are also radially distributed. At 12 μs, the backflow interacted with the discharge-induced flow in an approximately opposite direction, where the shear stress causes a vortex to form at about 1 mm downstream of the tip of the anode. At 16 ns, a corresponding secondary vortex is

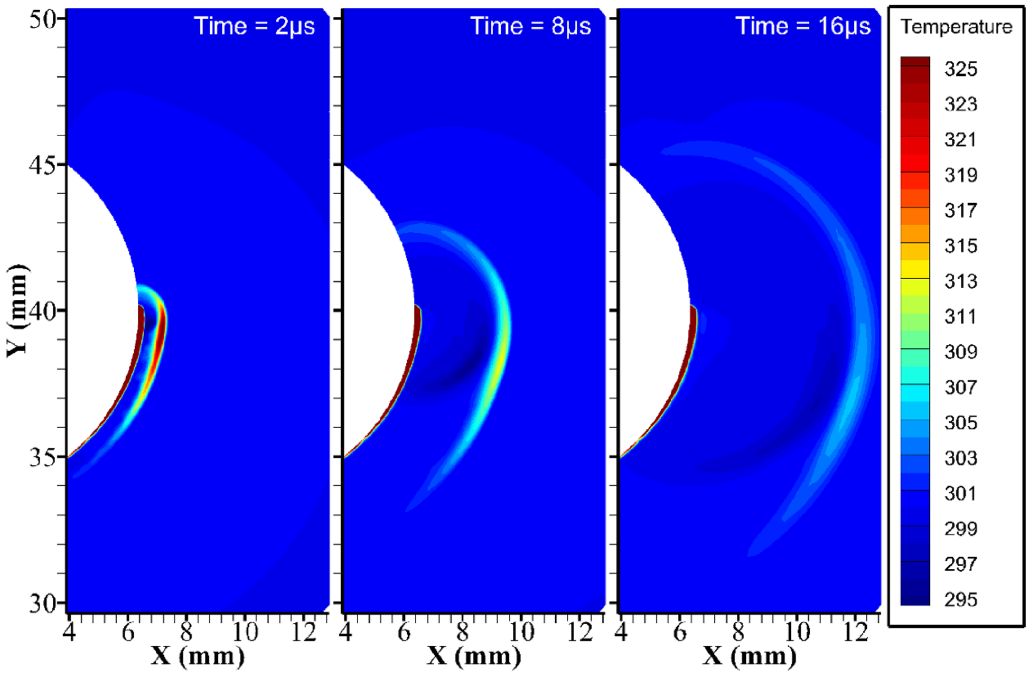

Figure 15. Temperature distribution at specific time moments.

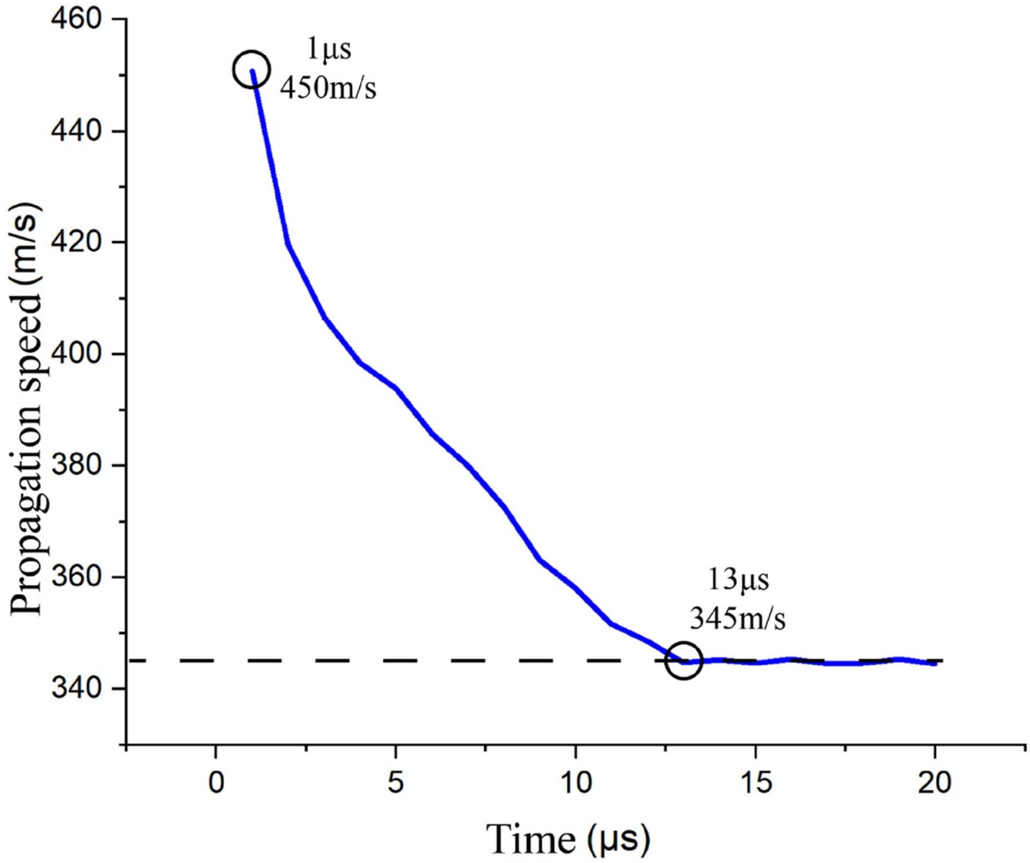

Figure 16. Evolution of the propagation speed of the compression wave.

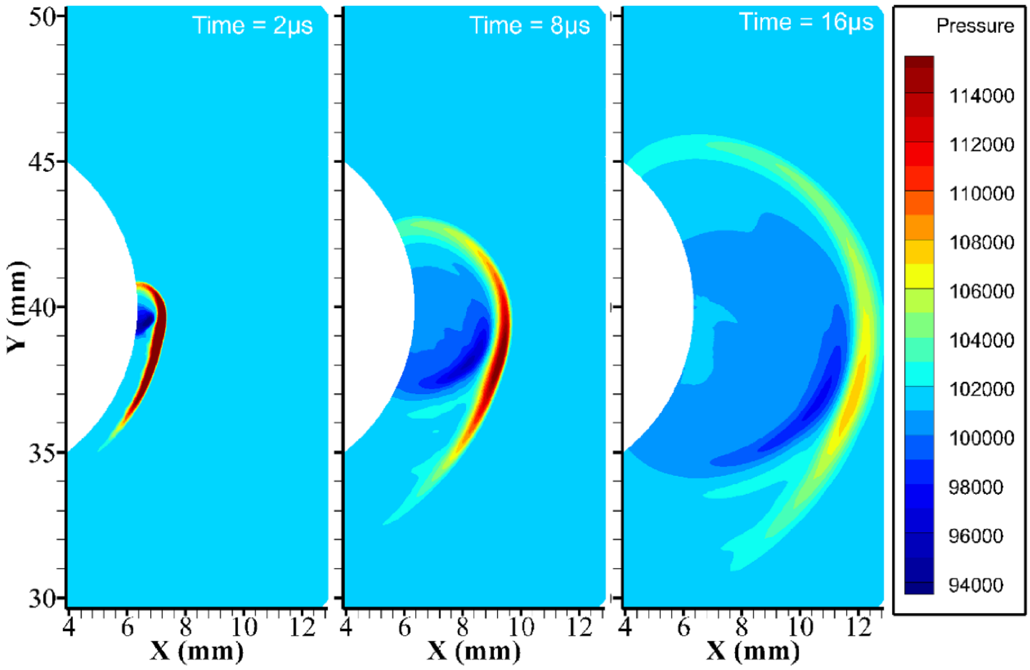

Figure 17. Pressure distribution at specific time moments.

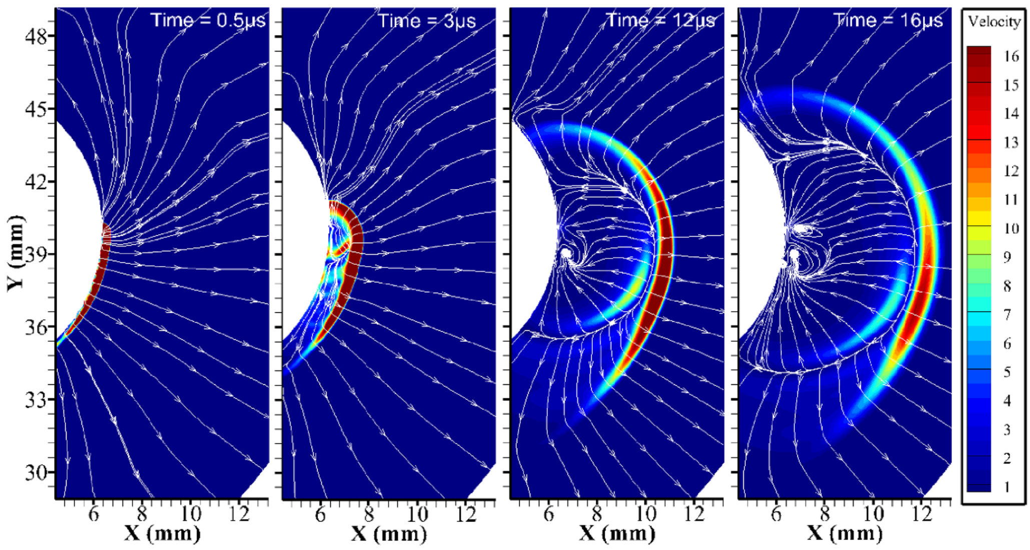

Figure 18. Velocity distribution with streamlines at specific time moments.

generated downstream of the vortex, which is closer to the wall. Another vortex is generated upon the tip of the anode after the previous one because of the relatively lower velocity of the backflow induced by a smaller pressure difference upon this vortex compared with that at the front.

5. Conclusions

A configuration of an NS-DBD actuator embedded in a curved dielectric layer is proposed and numerically studied on the streamer evolution and aerodynamic perturbations. The discharge characteristics are obtained by solving continuity equations that consider 15 species and 34 reactions, the energy conservation equation of electrons, and Poisson's equation, which is based on the drift–diffusion approximation. A single pulsed voltage with a pulse width of 35 ns and peak voltage of 14 kV applied on the anode is simulated, and the evolution of surface discharge is illustrated and analyzed. The one-way coupling strategy is employed to calculate the aerodynamic perturbations by putting a spatially distributed energy source into the compressible Navier–Stokes equations. The characteristics of temperature, pressure and velocity are also studied. Two-dimensional computation is performed, and the conclusions are summarized as follows.

For the discharge process, a surface-attached streamer is obtained for the curved configuration in this study. The streamer discharge is initiated at 2.2 ns and, until the end of the pulsed voltage, the electric field at the streamer head decreases. The maximum electric field is located at the streamer head, tip of the anode and inside the dielectric layer during the voltage-rise, plateau and decay stages correspondingly. The maximum electron number density sticks at the tip of the anode in the discharge process, and it increases and then remains constant in the voltage-rise and plateau stages, respectively, while the electron number density at the streamer head stays approximately constant. At the voltage-decay stage, the maximum electron number density decreases firstly and then increases due to the dominant quenching effect of excited species, which is consistent with the trend of the discharge power. The initial discharge propagation velocity is smaller than the flat NS-DBD, while the decrement is slower. In the entire discharge process, the discharge propagation velocity is positive, which results in a longer discharge length. The generation of discharge energy starts as the streamer initiates, and it reaches the peak as the voltage rises to the maximum. A similar trend of deposited energy distribution is obtained for both discharges, which demonstrates good agreement with the analytical solution.

For the excited flow field, the ambient atmospheric air is heated to 1883 K within 0.04 μs, and the rise of the maximum temperature remains greater than 1000 K and 500 K for 0.32 μs and 21.6 μs, respectively. A 'semiring-like' compression wave with a curved 'tail' parallel to the wall is formed. The compression wave propagates away from the wall; the propagation speed is initially about 450 m s^{-1} and then decreases progressively to 345 m s^{-1}, which is close to the speed of sound, and it remains approximately constant from 13 μs. High-speed flows are induced by the pressure difference in the flow field. When the compression wave propagates to a certain distance from the wall, backflows are induced and interact with the flows directly induced from the discharge region, which successively form two vortexes downstream and upon the tip of the anode, respectively.

Data availability statement

The data that support the findings of this study are available upon reasonable request from the authors.

Acknowledgments

This work is supported by the National Numerical Wind Tunnel Project of China (Grant Nos. NNW2019ZT7-B30 and NNW2018-ZT3B08).

ORCID iDs

Longfei Li https://orcid.org/0000-0001-9729-4663
Jiangfeng Wang https://orcid.org/0000-0003-4756-3858

References

[1] Corke T C, Enloe C L and Wilkinson S P 2010 *Annu. Rev. Fluid Mech.* **42** 505
[2] Cattafesta L N and Sheplak M 2011 *Annu. Rev. Fluid Mech.* **43** 247
[3] Wang J J, Choi K S, Feng L H, Jukes T N and Whalley R D 2013 *Prog. Aerosp. Sci.* **62** 52
[4] Corke T C, Post M L and Orlov D M 2007 *Prog. Aerosp. Sci.* **43** 193
[5] Jayaraman B and Shyy W 2008 *Prog. Aerosp. Sci.* **44** 139
[6] Shang J S and Huang P G 2014 *Prog. Aerosp. Sci.* **67** 29
[7] Starikovskaia S M 2014 *J. Phys. D: Appl. Phys.* **47** 353001
[8] Popov N A 2016 *Plasma Sources Sci. Technol.* **25** 043002
[9] Roupassov D V, Nikipelov A A, Nudnova M M and Starikovskii A Y 2009 *AIAA J.* **47** 168
[10] Breden D and Raja L L 2009 *40th AIAA Plasmadynamics Lasers Conf.* p 3594
[11] Roupassov D V, Nikipelov A A, Nudnova M M and Starikovskii A Y 2008 *46th AIAA Aerosp. Sci. Meet. Exhib.* p 1367
[12] Babaeva N Y, Tereshonok D V and Naidis G V 2016 *Plasma Sources Sci. Technol.* **25** 044008
[13] Ebato S, Ogino Y and Ohnishi N 2011 *49th AIAA Aerosp. Sci. Meet. Incl. New Horizons Forum Aerosp. Expo.* p 1142
[14] Likhanskii A V, Shneider M N, Opaits D F, Miles R B and Macheret S O 2010 *48th AIAA Aerosp. Sci. Meet. Incl. New Horizons Forum Aerosp. Expo.* p 470
[15] Gulati P, Prakash R, Pal U N, Geetha S S and Vyas V 2014 *IEEE Trans. Plasma Sci.* **42** 2266
[16] Enloe C L, Font G I, McLaughlin T E and Orlov D M 2008 *AIAA J.* **46** 2730
[17] Unfer T and Boeuf J P 2009 *J. Phys. D: Appl. Phys.* **42** 194017
[18] Starikovskii A Y, Nikipelov A A, Nudnova M M and Roupassov D V 2009 *Plasma Sources Sci. Technol.* **18** 034015
[19] Wang C C and Roy S 2012 *J. Appl. Phys.* **111** 103302
[20] Che X, Shao T, Nie W and Yan P 2012 *J. Phys. D: Appl. Phys.* **45** 145201
[21] Zhang S, Chen Z, Zhang B and Chen Y 2019 *J. Appl. Phys.* **125** 1
[22] Zhang S, Chen Z, Zhang B and Chen Y 2019 *Molecules* **24** 3933
[23] Xu S Y, Cai J S and Li J 2016 *Phys. Plasmas* **23** 103510
[24] Xu S Y, Cai J S, Zhang Z K and Tang S J 2017 *J. Phys. D: Appl. Phys.* **50** 185201
[25] Xu S Y, Cai J S, Wang J F and Tang S J 2020 *Contrib. Plasma Phys.* **60** 1
[26] Ahn S, Chae J, Kim H J and Kim K H 2017 *AIAA SciTech Forum—55th AIAA Aerosp. Sci. Meet.* p 1806
[27] Ahn S, Chae J, Kim H J and Kim K H 2021 *Int. J. Aeronaut. Space Sci.* **22** 547
[28] Zhang S, Chen Z, Zhang B and Chen Y 2019 *Appl. Sci.* **9** 5429
[29] Zhu Y, Wu Y, Cui W, Li Y and Jia M 2013 *J. Phys. D: Appl. Phys.* **46** 355205
[30] Zhu Y, Shcherbanev S, Baron B and Starikovskaia S 2017 *Plasma Sources Sci. Technol.* **26** 125004
[31] Zhu Y and Starikovskaia S 2018 *Plasma Sources Sci. Technol.* **27** 124007
[32] Zhu Y, Chen X, Wu Y, Hao J, Ma X, Lu P and Tardiveau P 2021 *Plasma Sources Sci. Technol.* **30** 075025
[33] Zhao G, Li Y, Liang H, Hua W and Han M 2015 *Acta Phys. Sin.* **64** 015101
[34] Li Y, Li J, Wu Y and Liu D 2015 *J. Aerosp. Power* **30** 537
[35] Wojewodka M M, White C, Ukai T, Russell A and Kontis K 2019 *Phys. Plasmas* **26** 1
[36] Takashima K, Yin Z and Adamovich I V 2013 *Plasma Sources Sci. Technol.* **22** 015013

[37] Zheng J G, Cui Y D, Zhao Z J, Li J and Khoo B C 2016 *Phys. Rev. Fluids* **1** 1
[38] Zheng J G, Zhao Z J, Li J, Cui Y D and Khoo B C 2014 *Phys. Fluids* **26** 1
[39] Luque A, Ebert U, Montijn C and Hundsdorfer W 2007 *Appl. Phys. Lett.* **90** 1
[40] Bourdon A, Pasko V P, Liu N Y, Célestin S, Ségur P and Marode E 2007 *Plasma Sources Sci. Technol.* **16** 656
[41] Kossyi I A, Kostinsky A Y, Matveyev A A and Silakov V P 1992 *Plasma Sources Sci. Technol.* **1** 207
[42] Pancheshnyi S, Nudnova M and Starikovskii A 2005 *Phys. Rev.* E **71** 1
[43] Popov N A 2011 *J. Phys. D: Appl. Phys.* **44** 285201
[44] Tholin F, Lacoste D A and Bourdon A 2014 *Combust. Flame* **161** 1235
[45] Hagelaar G J M and Pitchford L C 2005 *Plasma Sources Sci. Technol.* **14** 722
[46] Phelps A V and Pitchford L C 1985 *Phys. Rev.* A **31** 2932
[47] Lawton S A and Phelps A V 1978 *J. Chem. Phys.* **69** 1055
[48] Capitelli M, Ferreira C M, Gordiets B F and Osipov A I 2000 *Plasma Kinetics in Atmospheric Gases* (Berlin: Springer Science & Business Media)
[49] Schenk O and Ğartner K 2004 *Future Gener. Comput. Syst.* **20** 475
[50] Sonneveld P 1989 *SIAM J. Sci. Stat. Comput.* **10** 36
[51] Li J G 2008 *Mon. Weather Rev.* **136** 4709
[52] Verwer J G, Sommeijer B P and Hundsdorfer W 2004 *J. Comput. Phys.* **201** 61
[53] Kulikovsky A A 1998 *Phys. Rev.* E **57** 7066
[54] Stepanyan S A, Soloviev V R and Starikovskaia S M 2014 *J. Phys. D: Appl. Phys.* **47** 485201
[55] Li J W and Wang J F 2020 *Int. J. Mod. Phys.* B **34** 2040072
[56] Yang T P and Wang J F 2020 *Int. J. Mod. Phys.* B **34** 2040079
[57] Yang T, Wang J, Yang L and Shu C 2019 *Phys. Rev.* E **100** 1
[58] Yang T, Wang J, Yang L and Shu C 2020 *Comput. Fluids* **197** 104382
[59] Menter F R 1994 *AIAA J.* **32** 1598
[60] Liou M S 1995 *12th Comput. Fluid Dyn. Conf.* p 606
[61] Wieting A R 1987 *Experimental Study of Shock Wave Interference Heating on a Cylindrical Edge* (Washington, D.C)
[62] Lehr H F 1972 *Astronaut. Acta* **17** 589
[63] Abdollahzadeh M, Páscoa J C and Oliveira P J 2014 *Curr. Appl. Phys.* **14** 1160
[64] Tholin F and Bourdon A 2011 *J. Phys. D: Appl. Phys.* **44** 385203
[65] Soloviev V and Krivtsove V Analytical and Numerical Estimation of the Body Force and Heat Sources Generated by the Surface Dielectric Barrier Discharge Powered by Alternating Voltage, 6TH EUROPEAN CONFERENCE FOR AERONAUTICS AND SPACE SCIENCES (EUCASS)
[66] Zhu Y and Wu Y 2020 The secondary ionization wave and characteristic map of surface discharge plasma in a wide time scale *New Journal of Physics* **22**
[67] Soloviev V 2012 Analytical estimation of the thrust generated by a surface dielectric barrier discharge, Journal of physics *applied physics* **45**
[68] Soloviev V 2019 Analytical Model of a Surface Barrier Discharge Development *Plasma Physics Reports* **45** 246